Research Article | Vol. 9, No. 11 | 1 Nov 2018 | BIOMEDICAL OPTICS EXPRESS 5503
Biomedical Optics EXPRESS

Low-cost compact multispectral spatial frequency domain imaging prototype for tissue characterization

MOHSEN ERFANZADEH,[1] SREYANKAR NANDY,[2] PATRICK D. KUMAVOR,[1] AND QUING ZHU[2,3,*]

[1]*Department of Biomedical Engineering, University of Connecticut, Storrs, CT 06269, USA*
[2]*Department of Biomedical Engineering, Washington University in St. Louis, St. Louis, MO 63130, USA*
[3]*Department of Radiology, Washington University School of Medicine, St. Louis, MO 63110, USA*
[*]*zhu.q@wustl.edu*

Abstract: We present a low-cost, compact, and multispectral spatial frequency domain imaging prototype. Illumination components, including 9 LEDs (660 nm – 950 nm) placed on a custom-designed printed circuit board, linear and rotational motors, a printed sinusoidal pattern, and collimation and projection optics as well as the detection components are incorporated in a compact custom-designed 3D-printed probe. Reconstruction of absorption and reduced scattering coefficients is evaluated via imaging tissue mimicking phantoms and potentials of the probe for biological tissue imaging are evaluated via imaging human ovarian tissue *ex vivo*.

1. Introduction

Optical properties of tissue may vary in healthy and diseased conditions, therefore optical imaging modalities capable of providing quantitative maps of absorption and scattering properties can assist in characterization of healthy versus diseased tissue [1,2]. Spatial frequency domain imaging (SFDI) is a wide-field diffuse optical imaging modality that can quantitatively map various optical properties of tissue and has shown potentials in differentiating benign and malignant tissue in several cancer types including breast and ovarian cancer [1–6].

In SFDI, tissue is illuminated with sinusoidal (or square [7]) spatially modulated light and optical properties of the target are reconstructed using the diffusely backscattered light collected by a camera [4,5]. Initial reports of SFDI systems utilized general-purpose projectors, with built-in digital micro-mirror devices (DMDs), to project the spatially sinusoidal patterns, generated from a computer connected to the projector, on the tissue [3–5,8]. External optical filters were used to select the desired wavelength [3,5] and filters could be manually or mechanically switched to use different wavelengths. Later versions of SDFI systems utilize LEDs collimated and co-aligned by multiple collimating lenses, beam splitters, and dichroic mirrors [1,9]. An external DMD controlled by a PC [1], or a printed sinusoidal pattern [9] provide the spatial modulation of light that is then projected on the tissue. Such systems generally utilize four LEDs [1]. Incorporating and co-aligning larger number of LEDs in such setups requires many optical components which increase the size, cost, and complexity of the system. Albeit, a system incorporating a 6-wavelength SFDI head using custom-made fibers, fiber couplers, and a fiber bundle multiplexer to combine all LED lights has been reported previously. That system, however, is relatively large and contains various components that increase its cost [10], which can affect the point-of-care applications and clinical applications at areas with low-resource settings [11,12]. Applications of digital light projectors (DLPs) as the source for SFDI systems have also been reported [13,14]. In visible DLPs, which are the more common versions, RGB LEDs are collimated and co-

#335885 https://doi.org/10.1364/BOE.9.005503
Journal © 2018 Received 22 Jun 2018; revised 4 Sep 2018; accepted 4 Oct 2018; published 17 Oct 2018
Corrected: 23 October 2018

Biomedical Optics EXPRESS

aligned using collimator lenses, beam splitters, and dichroic mirrors and the projection pattern is generated by a DMD [13]. Although common (hence, less expensive) DMDs are often sensitive to the visible light, modified DLPs with near infrared (NIR) LEDs or laser diodes are also available [15]. However, either visible or NIR DLPs only use three fixed wavelengths while utilizing a larger number of wavelengths from visible to NIR enhances SFDI studies of biological tissues [13,15]. Here, we report a low-cost, compact, 3D-printed SFDI prototype incorporating nine different LEDs (wavelengths from 660 nm – 950 nm) with all illumination and detection components in a compact probe. Comparison between the proposed prototype and the previously reported SFDI systems is summarized in Table 1. Reconstruction of absorption coefficient (μ_a) and reduced scattering coefficient (μ_s') are evaluated via imaging tissue mimicking phantoms. Finally, human ovarian tissue samples are imaged and analyzed using the proposed SFDI probe.

Table 1. Comparison of the proposed SFDI probe with previously reported examples

SFDI system	Wavelengths	Compact (Y/N)	Cost
Initial projector-based system [3–5,8]	Single (increased by additional filters)	N	Low to Medium
Systems utilizing co-aligned LEDs [1,9]	4	N	Medium
SFDI head with custom-made fibers [10]	6	N	High
DLP-based SFDI systems [13,14]	3	Y	Medium
The proposed prototype in this report	9	Y	Low

2. Methods

2.1 SFDI prototype

A schematic representation of the SFDI prototype is shown in Fig. 1(a). The illumination portion of the prototype consists of a rotational stepper motor (PG20L-D20-HHC0, NMB Technologies), 9 LEDs with peak emission wavelengths ranging from 660 nm – 950 nm placed on a custom-designed printed circuit board (PCB), a light diffuser, an achromatic doublet collimating lens (Thorlabs, AC254-050-B-ML), a printed sinusoidal pattern, a linear stepper motor (19541-12-905, Ametek), and an achromatic doublet projection lens (Thorlabs, AC254-050-B-ML). On the PCB, LEDs are placed on the circumference of a circle with a fixed distance and the rotational motor rotates the PCB in order to switch the LED that is positioned on the optical axis of the lenses. Peak emission wavelengths of the LEDs are at ~660 nm (± 12.5 nm half power spectral width), 740 nm (± 15 nm), 780 nm (± 12.5 nm), 810 nm (± 20 nm), 830 nm (± 20 nm), 850 nm (± 20 nm), 890 nm (± 20 nm), 935 nm (± 25 nm), and 950 nm (± 21 nm) and the LEDs have either 50 mA or 100 mA maximum forward current. Light from the LED first passes through a beam diffuser to homogenize the beam and is then collimated by the collimating lens. The degree of beam diffusion, the focal length of the collimating lens, and the distance between the diffuser and collimator are chosen to minimize energy loss and yet maintain suitable homogenization and collimation of light. The collimated beam passes the printed pattern and is projected on the sample using the projector lens. The 2D sinusoidal pattern, generated in MATLAB (Mathworks, Natick, MA, USA), was printed on a transparency paper in order to significantly reduce the probe cost compared to using DMDs or even commercially available printed patterns. Considering the color resolution of a general purpose printer, by adjusting the colors assigned to the maximum and minimum of the generated sine function, the pattern was empirically modified such that the one dimensional profile of the pattern detected by the camera was closest to a sinusoidal function for different phantoms. The focal length of the projector lens and the distance between the projector lens and the pattern are chosen such that the pattern is best projected on the target at the desired distance. The printed pattern is attached to the linear motor that provides the phase shift between the patterns shining on the tissue. Diffuse backscattered light is collected by a CMOS camera (EO-0413M-GL, Edmund Optics). Two polarizer plates are

Biomedical Optics EXPRESS

located at the illumination and detection sides in order to reject specular reflection. The illumination area is a circle with a diameter of about 13 cm approximately 30 cm away from the probe, however the detection field of view is about 5 cm × 4 cm at this distance. Control and synchronization of LEDs, motors, and data acquisition are performed in a custom-made LabVIEW code (National Instrument, Austin, TX, USA) combined with Arduino IDE (Arduino, Italy). The communication with the PC is performed through a serial USB port. Complete data acquisition for all wavelengths lasts for approximately 2 minutes.

All pieces are fixed and aligned in a 3D-printed probe designed in Solidworks (Solidworks, Waltham, MA, USA). As shown in Fig. 1(b), the illumination section of the probe is 17 cm × 6 cm × 6 cm (length × width × height). The camera is held by a piece designed to fix and align the camera with the illumination light and allow for minor modifications. The camera holder consists of an adaptor 6 cm × 6 cm × 1 cm (Fig. 1(c)) that is fixed to the illumination probe, a second adaptor 6 cm × 7 cm × 6 cm (Fig. 1(d)) that is screwed to the first adaptor, and a hollow cube of 8 cm × 5 cm × 5 cm (Fig. 1(e)) that holds the camera and is screwed to the second adaptor in order to provide a degree of freedom for adjusting the imaging area. The camera holder part is completely fixed on top of the illumination part and the entire probe can be held by hand or simply fixed to a table. The complete probe is shown in Fig. 1(f). The list and cost of the illumination components and the probe are summarized in Table 2. Given that a detection camera is common among all SFDI systems, it is not included in this table. Moreover, the costs mentioned in the table are based on the retail price of the components which are usually considerably higher than the wholesale prices.

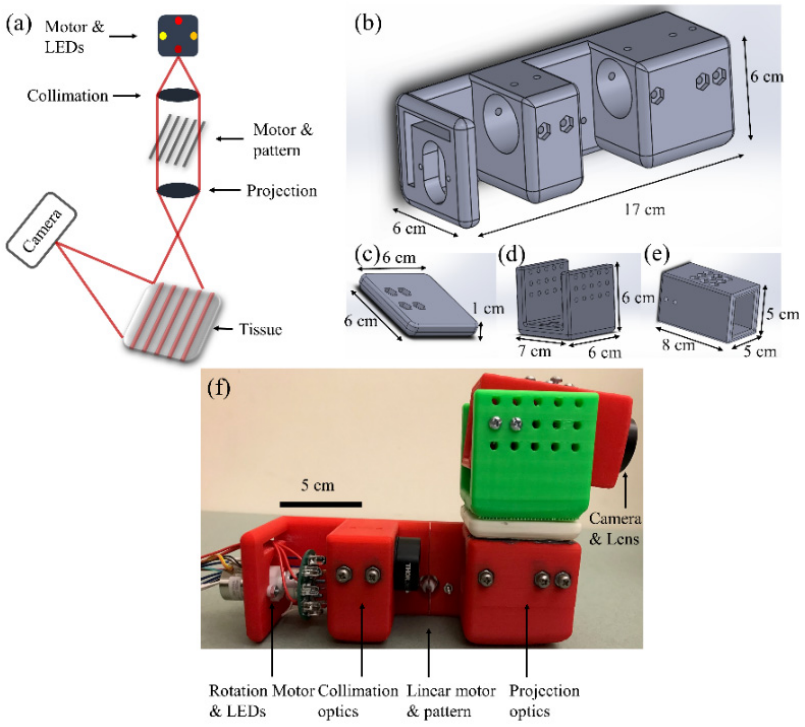

Fig. 1. (a) Schematic representation of the SFDI probe. (b-e) SolidWorks designs of the probe pieces. (f) The 3D-printed SFDI probe.

The spatial frequency used for the current study was 1 cm^{-1}. The reconstruction algorithm is similar to the previously reported methods [3,5,14]. Briefly, for each wavelength, three

Biomedical Optics EXPRESS

phase-shifted (0, 2π/3, and 4π/3) patterns are shined on the target and are detected by the camera. Using the phase shifted patterns, the DC (spatial frequency = 0 cm^{-1}) and AC (spatial frequency = 1 cm^{-1}) components of the diffused reflected light are extracted using amplitude demodulation [5]. Prior to imaging the target, a calibrated reference phantom is also imaged at the same illumination condition and DC and AC components of the diffused reflected light from the phantom are also extracted. The diffuse reflectance components from the target are then calibrated using those from the reference and the theoretical expected value from the reference [5]. This results in two calibrated diffuse reflectance values, DC with 0 cm^{-1} and AC with 1 cm^{-1} spatial frequencies. Using the two diffuse reflectance maps and calculated lookup tables, absorption coefficient and reduced scattering coefficient values are calculated for each pixel [5,14]. Moreover, effort is made to limit the height mismatch between the phantom and the sample to minimize its effects on reconstructed values.

Table 2. Cost of the illumination components and the probe

Illumination Component	Approximate Cost (USD)
Rotational motor	40
PCB	5
LEDs (combined)	15
Diffuser	30
Achromatic doublet collimator lens	110
Linear motor	75
Pattern	3
Achromatic doublet projection lens	110
3D printing material	25
Total cost of illumination components and the probe	413

2.2 Human ovarian samples

Informed consent was obtained from patients undergoing oophorectomy for imaging the freshly excised ovarian tissue at Washington University School of Medicine. The study was approved by the Institutional Review Board (IRB) at Washington University (201608016). Imaging was performed in less than one hour after the surgery and the samples were returned to the pathology department after the imaging.

3. Results and discussions

3.1 Phantom evaluation

Liquid phantoms were made using Indian ink as the absorber and Intralipid as the scattering agent. Collimated transmission setup was used to separately measure the absorption and scattering coefficients of parent ink and Intralipid solutions, respectively, and the absorption coefficient and reduced scattering coefficient of diluted phantoms were estimated using titration equation and reported anisotropy factor of Intralipid and absorption of water in the literature [16–20]. Figure 2 shows an example of the reconstructed and expected values for absorption coefficient (a) and reduced scattering coefficient (b) for a liquid phantom for all wavelengths of the probe.

Table 3 lists the evaluated phantoms and the average error in μ_a and μ'_s considering all wavelengths for each phantom. Phantoms were made at different μ_a and μ'_s values in order to evaluate the sensitivity of the probe to the changes in absorption and scattering coefficients. Similar values of μ_a and μ'_s were used for phantoms in calibration of SFDI systems used for characterization of ovarian tissue [3]. Please note that μ_a and μ'_s are different at each wavelength but in the table we only provide the expected values at 810 nm to distinguish between the phantoms. The absolute average error was approximately 6.7 ± 4.9% (average ± std) for μ_a and 4.7 ± 3.7% for μ'_s, considering all wavelengths and all phantoms. The variations in errors between different phantoms could rise from different inaccuracies in phantom preparation in addition to the inherent system and reconstruction error. Because μ_a

Biomedical Optics EXPRESS

values are smaller compared to μ'_s, the relative error in μ_a reconstruction is more sensitive to the interpolation error between the mesh grids of the lookup table, which sometimes results in different relative error percentages between μ_a and μ'_s reconstruction.

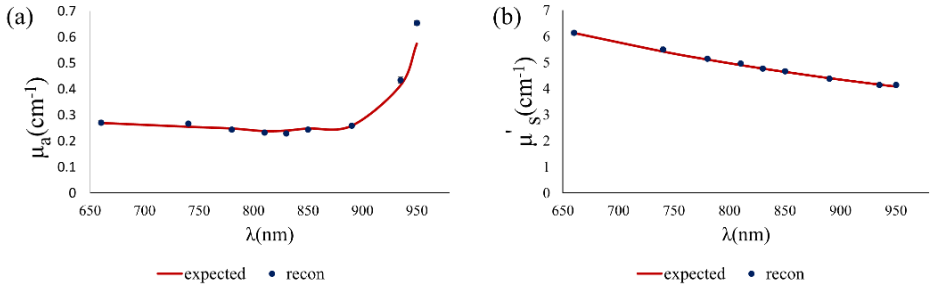

Fig. 2. An example of reconstructed absorption coefficient (a) and reduced scattering coefficient (b) for a liquid phantom (phantom #3 in Table 1) for all wavelengths in the probe.

Table 3. Phantoms used for SFDI probe evaluation

Phantom #	Expected μ_a @ 810 nm (cm^{-1})	Average μ_a error for all λs (%)	Expected μ'_s @ 810 nm (cm^{-1})	Average μ'_s error for all λs (%)
1 (ref)	0.0745	0.19	4.9056	0.22
2	0.1293	2.40	4.9056	2.82
3	0.2387	3.87	4.9056	0.72
4	0.0745	9.82	6.8678	9.77
5	0.0745	13.66	7.5546	8.08
6	0.0745	10.52	9.8112	6.43

3.2 Ovarian tissue

Figure 3 shows the photographs, absorption coefficient maps (at 660 nm), reduced scattering coefficient maps (at 660 nm), and scattering slope maps (power law dependence of scattering on wavelengths as explained previously in Ref [21].) for two benign human ovarian tissue samples *ex vivo* (O#1, 2). The average reconstructed values for the ovaries are within the expected range for biological tissue [14,22]. For instance, in a previous study using a frequency domain diffused light system at 780 nm, absorption coefficient of 33 *ex vivo* ovaries were measured and the range was between 0.006 cm^{-1} and 0.18 cm^{-1} [22]. The fact that no major heterogeneity in scattering slope maps are noticed within either ovaries can be traced to the fact that tissue structure is not considerably altered throughout the ovary. We also imaged an ovarian tissue with a large water-filled cyst (O#3). Using the ratio of absorption maps at 950 nm (strong water absorption, Fig. 4(c)) and a visible wavelength (e.g. 660 nm, negligible water absorption and mainly collagen and blood absorption, Fig. 4(b)), water-collagen content ratio can be obtained and it can be used to distinguish ovaries with large water-filled cysts. This distinction is clearly visible in Fig. 4(d) that compares this ratio for the three ovaries. This method can help to reduce ambiguity for potential *in vivo* applications when a patient develops a large cystic ovary.

Biomedical Optics EXPRESS

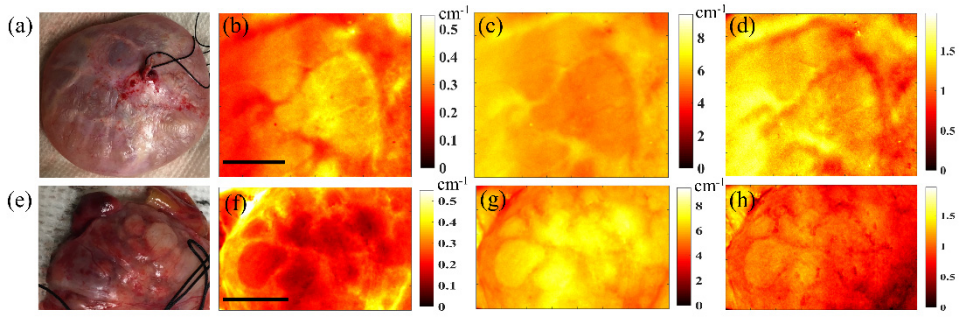

Fig. 3. Photographs (a, e), absorption coefficient maps at 660 nm (b, f), reduced scattering coefficient maps at 660 nm (c, g), and scattering slope maps (d, h) of two benign ovarian tissues (top row: O#1, bottom row: O#2). The scale bars are 1 cm.

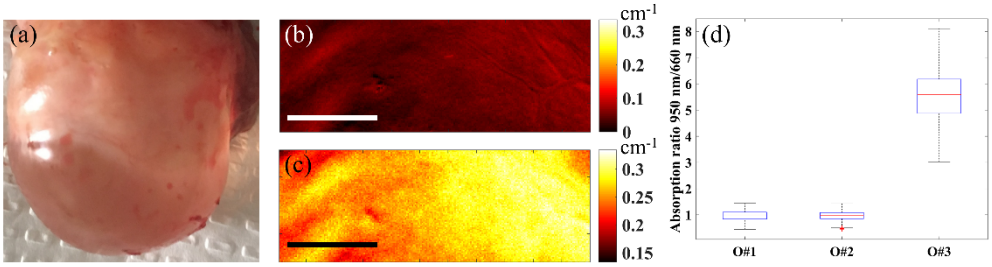

Fig. 4. Photograph (a), absorption coefficient map at 660 nm (b), and absorption coefficient map at 950 nm (c) of ovary #3, and comparison ratio of absorption at 950 nm and 660 nm for ovaries 1-3 (d). The scale bars are 0.5 cm.

Figure 5 shows the average absorption coefficients at all wavelengths for the three ovaries. The diagnosis of the two benign ovaries from the same 65-year-old postmenopausal patient are serous cystadenofibroma (O#1) and mucinous cyctadenoma (O#2). The absorption spectra measured from these two benign ovaries of the same patient could be the mixed spectra of collagen, deoxy hemoglobin (Hb), oxy-hemoglobin (HbO2), and lipid (mainly for 935 nm) [23,24]. Reviewing of the H&E stains (Hematoxylin and Eosin) of serous cystadenofibroma showed dense collagen and more scattered blood vessels, and mucinous cyctadenoma showed densely packed collagen and also some scattered blood vessels. The two benign ovarian tissue absorption spectra follow collagen absorption spectrum from 660 to 740nm, as collagen absorption dominates that of Hb and HbO_2 in this range [24]. On the other hand, ovary 3 has a completely different absorption pattern which is low at shorter wavelengths and starts to grow at longer wavelengths with a sharp increase in the mid-900 nm range, consistent with absorption of water. This further indicates the potentials of multispectral SFDI systems with wavelengths within the optical window and slightly beyond for characterization of ovarian tissue. For ovaries 1 and 2, the 935 nm LED light shows a higher absorption value compared to the 950 nm light; this may be because in addition to lipid, water also has noticeable absorption at the vicinity of 935 nm [19,20,23]. The ovarian surface of the serous cystadenofibroma has a 4.0 cm white-pink nodular mass and the mucinous cyctadenoma surface is white-pink smooth surface. This suggests that both ovarian tissue surfaces have lipid and water content. Moreover, as both 935 and 950 nm LEDs have about ± 20 nm spectral width, the measurements are smoothed or averaged spectra. This, however, does not affect the analysis of comparing the water content of tissue samples using the 950 nm absorption and a visible wavelength. However, we do note that studying a larger number of samples with various abnormalities and malignant lesions will provide a more comprehensive understanding of the absorption spectrum of ovarian tissue.

Biomedical Optics EXPRESS

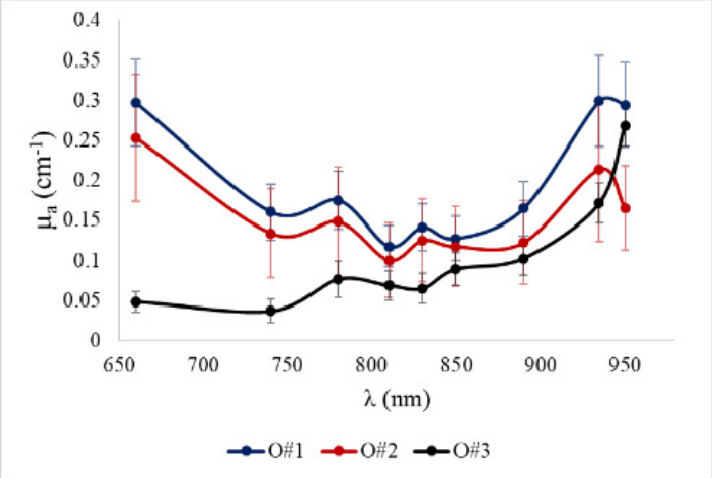

Fig. 5. Average absorption coefficient of three ovarian tissues for all wavelengths.

4. Conclusions

We reported the design and implementation of a low-cost, compact, and multispectral SFDI system incorporating all illumination and detection components in a small 3D-printed probe. Reconstruction of absorption and reduced scattering coefficients are evaluated using tissue mimicking phantoms. Human ovarian tissues are imaged *ex vivo* to demonstrate the potential of the probe for imaging and analyzing biological tissue. Studying a larger pool of benign and malignant ovarian and colorectal cancer samples using the proposed probe and implementing feature extraction algorithms on the obtained SFDI data is a study we are currently pursuing. Moreover, with modifications in illumination components and incorporating micro-cameras, this simple prototype design can be further miniaturized. The probe in its current form is designed to be handheld, however hand movements during the acquisition can potentially create artifacts and affect reconstructed values. Increasing the acquisition speed using higher speed motors and implementing motion artifact compensation techniques can help facilitate handheld clinical applications of the system. Designs implementing a (tunable) broadband source and/or a tunable filter instead of the rotating motor and multiple LEDs could also increase the acquisition speed.

Funding

National Institute of Health (NIH) (R01CA151570); Connecticut Innovations Bioscience Pipeline award.

Acknowledgements

Dr. Ian Hagemann and Drs. Matthew Powell and Lindsay Kuroki from the department of Pathology and Obstetrics & Gynecology at Washington University School of Medicine are sincerely thanked for their help on tissue sample and patient recruitment. Helps from Ruth Holdener and Lynne Lippmann from Radiology and Gynecologic Oncology division at Washington University School of Medicine for obtaining patient consent and study coordination is also acknowledged.

Disclosures

The authors declare that there are no conflicts of interest related to this article.

Biomedical Optics EXPRESS

References

1. A. M. Laughney, V. Krishnaswamy, E. J. Rizzo, M. C. Schwab, R. J. Barth, Jr., D. J. Cuccia, B. J. Tromberg, K. D. Paulsen, B. W. Pogue, and W. A. Wells, "Spectral discrimination of breast pathologies in situ using spatial frequency domain imaging," Breast Cancer Res. **15**(4), R61 (2013).
2. S. Tabassum, Y. Zhao, R. Istfan, J. Wu, D. J. Waxman, and D. Roblyer, "Feasibility of spatial frequency domain imaging (SFDI) for optically characterizing a preclinical oncology model," Biomed. Opt. Express **7**(10), 4154–4170 (2016).
3. S. Nandy, A. Mostafa, P. D. Kumavor, M. Sanders, M. Brewer, and Q. Zhu, "Characterizing optical properties and spatial heterogeneity of human ovarian tissue using spatial frequency domain imaging," J. Biomed. Opt. **21**(10), 101402 (2016).
4. D. J. Cuccia, F. Bevilacqua, A. J. Durkin, and B. J. Tromberg, "Modulated imaging: quantitative analysis and tomography of turbid media in the spatial-frequency domain," Opt. Lett. **30**(11), 1354–1356 (2005).
5. D. J. Cuccia, F. Bevilacqua, A. J. Durkin, F. R. Ayers, and B. J. Tromberg, "Quantitation and mapping of tissue optical properties using modulated imaging," J. Biomed. Opt. **14**(2), 024012 (2009).
6. S. Nandy, M. Erfanzadeh, F. Zhou, and Q. Zhu, "Feasibility study of spatial frequency domain imaging using a handheld miniaturized projector and rigid endoscope," in *Progress in Biomedical Optics and Imaging - Proceedings of SPIE* (2017), **10059**.
7. K. P. Nadeau, T. B. Rice, A. J. Durkin, and B. J. Tromberg, "Multifrequency synthesis and extraction using square wave projection patterns for quantitative tissue imaging," J. Biomed. Opt. **20**(11), 116005 (2015).
8. S. D. Konecky, A. Mazhar, D. Cuccia, A. J. Durkin, J. C. Schotland, and B. J. Tromberg, "Quantitative optical tomography of sub-surface heterogeneities using spatially modulated structured light," Opt. Express **17**(17), 14780–14790 (2009).
9. M. Torabzadeh, I.-Y. Park, R. A. Bartels, A. J. Durkin, and B. J. Tromberg, "Compressed single pixel imaging in the spatial frequency domain," J. Biomed. Opt. **22**(3), 030501 (2017).
10. S. Gioux, A. Mazhar, B. T. Lee, S. J. Lin, A. M. Tobias, D. J. Cuccia, A. Stockdale, R. Oketokoun, Y. Ashitate, E. Kelly, M. Weinmann, N. J. Durr, L. A. Moffitt, A. J. Durkin, B. J. Tromberg, and J. V. Frangioni, "First-in-human pilot study of a spatial frequency domain oxygenation imaging system," J. Biomed. Opt. **16**(8), 086015 (2011).
11. M. Erfanzadeh, P. D. Kumavor, and Q. Zhu, "Laser scanning laser diode photoacoustic microscopy system," Photoacoustics **9**, 1–9 (2018).
12. C. T. Lam, M. S. Krieger, J. E. Gallagher, B. Asma, L. C. Muasher, J. W. Schmitt, and N. Ramanujam, "Design of a Novel Low Cost Point of Care Tampon (POCkeT) Colposcope for Use in Resource Limited Settings," PLoS One **10**(9), e0135869 (2015).
13. A. J. Lin, A. Ponticorvo, S. D. Konecky, H. Cui, T. B. Rice, B. Choi, A. J. Durkin, and B. J. Tromberg, "Visible spatial frequency domain imaging with a digital light microprojector," J. Biomed. Opt. **18**(9), 096007 (2013).
14. S. Nandy, I. S. Hagemann, M. A. Powell, C. Siegel, and Q. Zhu, "Quantitative multispectral *ex vivo* optical evaluation of human ovarian tissue using spatial frequency domain imaging," Biomed. Opt. Express **9**(5), 2451–2456 (2018).
15. EKB technologies, "Light Crafter MK II," http://www.ekb.co.il/lightcrafter-mk2.html.
16. R. Michels, F. Foschum, and A. Kienle, "Optical properties of fat emulsions," Opt. Express **16**(8), 5907–5925 (2008).
17. S. T. Flock, S. L. Jacques, B. C. Wilson, W. M. Star, and M. J. C. van Gemert, "Optical properties of Intralipid: A phantom medium for light propagation studies," Lasers Surg. Med. **12**(5), 510–519 (1992).
18. M. A. Ansari, M. Erfanzadeh, S. Alikhani, and E. Mohajerani, "Study of the effect of mechanical pressure on determination of position and size of tumor in biological phantoms," Appl. Opt. **52**(12), 2739–2749 (2013).
19. K. F. Palmer and D. Williams, "Optical properties of water in the near infrared," J. Opt. Soc. Am. **64**(8), 1107–1110 (1974).
20. W. Irvine and J. Pollack, "Infrared optical properties of water and ice spheres," Icarus **8**(4), 324–360 (1968).
21. A. M. Laughney, V. Krishnaswamy, T. B. Rice, D. J. Cuccia, R. J. Barth, B. J. Tromberg, K. D. Paulsen, B. W. Pogue, and W. A. Wells, "System analysis of spatial frequency domain imaging for quantitative mapping of surgically resected breast tissues," J. Biomed. Opt. **18**(3), 036012 (2013).
22. A. Aguirre, Y. Ardeshirpour, M. M. Sanders, M. Brewer, and Q. Zhu, "Potential Role of Coregistered Photoacoustic and Ultrasound Imaging in Ovarian Cancer Detection and Characterization," Transl. Oncol. **4**(1), 29–37 (2011).
23. P. Taroni, "Diffuse optical imaging and spectroscopy of the breast: A brief outline of history and perspectives," Photochem. Photobiol. Sci. **11**(2), 241–250 (2012).
24. S. K. V. Sekar, I. Bargigia, A. D. Mora, P. Taroni, A. Ruggeri, A. Tosi, A. Pifferi, and A. Farina, "Diffuse optical characterization of collagen absorption from 500 to 1700 nm," J. Biomed. Opt. **22**(1), 015006 (2017).